GEOMETRIC OPTIMIZATION OF A SELF-ADAPTIVE ROBOTIC LEG

Dmitri Fedorov[1] [2], Lionel Birglen[1]

[1]*Department of Mechanical Engineering, École Polytechnique de Montréal, Montréal, QC, Canada*

Email: dmitri.fedorov@polymtl.ca; lionel.birglen@polymtl.ca

ABSTRACT

Inspired by underactuated mechanical fingers, this paper demonstrates and optimizes the self-adaptive capabilities of a 2-DOF Hoecken's-Pantograph robotic leg allowing it to overcome unexpected obstacles encountered during its swing phase. A multi-objective optimization of the mechanism's geometric parameters is performed using a genetic algorithm to highlight the trade-off between two conflicting objectives and select an appropriate compromise. The first of those objective functions measures the leg's passive adaptation capability through a calculation of the input torque required to initiate the desired sliding motion along an obstacle. The second objective function evaluates the free-space trajectory followed by the leg endpoint using three criteria: linearity, stance ratio, and height-to-width. In comparison with the initial geometry based on the Hoecken's linkage, the selected final mechanism chosen from the Pareto front shows an important improvement of the adaptation capabilities, at the cost of a slight decrease in the stance phase duration. This paper expands on mechanical self-adaptive design philosophy, which recently attracted a lot of attention in the field of grasping, to legged locomotion and paves the way for subsequent experimental validation of this approach.

Keywords: optimization; robotic leg; underactuation; linkage; kinetostatic analysis.

RÉSUMÉ

En utilisant une approche similaire aux mécanismes de doigts sous-actionnés, les capacités d'adaptation d'une architecture de jambe robotique à deux DDL de type Hoecken's-Pantographe sont optimisées dans cet article afin de lui permettre de surmonter des obstacles imprévus lors de sa phase de vol. Une optimisation multiobjectif des paramètres géomtriques du mécanisme a été effectuée afin de mettre en évidence l'opposition existant entre deux objectifs contradictoires et choisir un compromis. Le premier de ces objectifs

[2] Corresponding author

mesure la capacité d'adaptation passive de la jambe en calculant le couple d'entrée requis pour amorcer le glissement désiré le long d'un obstacle. La deuxième fonction objectif évalue la trajectoire de base suivie par l'extrémité de la jambe en se basant sur trois critères : linéarité, ratio de la phase de support, et rapport hauteur/largeur. En comparaison avec la géométrie initiale pasée sur le mécanisme de Hoecken, le mécanisme final trouvé sur le front de Pareto présente une amélioration marquée des capacités d'adaptation, au coût d'une légère réduction de la durée de la phase de support. Cet article étend la philosophie de l'auto-adaptation mécanique, qui a récemment beaucoup attiré l'attention dans le domaine de la préhension, à celui de la marche, et ouvre la voie à une validation expérimentale de cette approche.

Mots-clés : optimisation ; jambe robotique ; sous-actionnement ; mécanisme à membrures ; analyse cinétostatique.

1. INTRODUCTION

While the simplicity, energy efficiency, and speed of wheeled locomotion are hard to match, walking robots are often a preferred alternative when navigating uneven terrains. Successful robotic leg designs are often serial mechanisms comprised of several actuated joints, such as in the Starl*ETH* (Hutter et al., 2012) or the HyQ (Semini et al., 2011) robots, or consist of much simpler compliant links, which, despite their simplicity, generate a very efficient dynamical gait for the robot and help successful navigation in rough terrains, as exemplified by the RHex (Saranli et al., 2001). On the other hand, mechanical linkages can also guide the endpoint of a robotic leg using as few as a single actuator and are largely unaffected by the payload while in stance phase conversely to designs using compliant links. However, while the limited number of actuators required with the designs based on linkages is a significant advantage, it is impossible for the leg to depart from the generated trajectory if the presence of an obstacle requires an adaptation. Active reconfiguration with the use of additional actuators has however been previously proposed, notably for the Theo Jansen linkage (Nansai et al., 2015).

Among linkages able to generate a suitable leg trajectory for a walking application, the combination of the Hoecken's linkage, also sometimes referred to as Chebyshev's lambda mechanism, and a pantograph for amplification purposes has been studied by many (Ottaviano et al., 2005; Tao and Ceccarelli, 2011; Liang et al., 2012), including the authors (Fedorov and Birglen, 2017). In the present paper, the geometric parameters of a two degree-of-freedom (DOF) variant of this architecture are, for the first time, optimized to take advantage of its self-adaptive capabilities. The desired objective is to allow the leg to "give in" without any sensing or control and slide along an obstacle following an unexpected collision, rather than trying to pursue an unfeasible trajectory. While a similar behaviour has been previously obtained by making use of electronic reflex generation (Park et al., 2013; Focchi et al., 2013), this effect is here intended to be obtained purely mechanically. It should be emphasized that, in our case, the leg does not avoid the collision with the obstacle, and that it remains in contact with the colliding object during the whole adaptation sequence.

The proposed approach is directly inspired by the design of self-adaptive mechanisms in the field of underactuated robotic hands (Birglen et al., 2008; Birglen, 2009): a single input force is distributed to several output phalanges, the motions of which are triggered by contacts between the finger and the grasped object. With the use of preloaded springs and mechanical limits, the closing sequence of the phalanges can

be achieved without any control or sensors. Similarly, a contact during the swing phase of the proposed leg mechanism passively triggers the secondary DOF which allows the leg to depart from its trajectory to accommodate the obstacle.

Ultimately, using a purely mechanical solution to generate a complex behaviour, such as obstacle overcoming, can be more affordable than relying on the complex software control of multiple actuators, and could prove to be useful for applications where environmental factors such as extreme temperatures or radiation impact the use of electronic controllers. Similar considerations have guided the recent emergence of underactuated grippers as affordable solutions for the grasping of complex objects. The expansion of this design philosophy to other applications might prove to be fruitful, as initially investigated in (Khakpour et al., 2014) for cable robots and is further investigated here.

2. MECHANISM DESCRIPTION

2.1. Geometry

The leg mechanism described in this paper can be separated in two basic linkages: a four-bar linkage acting as a path generator, and a pantograph. More specifically, the geometric parameters of the four-bar are initially matching the ones of the Hoecken's linkage, although they will be altered following the optimization described in Section 4. When driven by the rotation θ_1 of the input crank, this linkage generates a trajectory M_1 suitable for a walking application due to the existence of a linear portion and the proportion of the cycle (close to 70%) that is spent in this phase, as illustrated in Fig. 1a. The second element of the mechanism is the pantograph, *i.e.*, a linkage characterized by a constant ratio of the distance between its two *guiding points* to the distance between either of its *guiding points* and its *following point*, see Fig. 1a. The pantograph performs three functions in the mechanism, listed here by increasing order of importance for our application:

1. Amplify the trajectory M_1, which is inputed to one of the pantograph's guiding points.
2. Ensure that the leg endpoint (*i.e.*, the following point) is the lowest point of the mechanism.
3. Add a second degree of freedom, θ_2, to the mechanism. The associated motion M_2 is applied to the pantograph's second guiding point, and therefore, also affects the position of the following point.

2.2. Self-adaptive behaviour

As is often the case with self-adaptive fingers where the motion of a phalanx may not be triggered until contact is established with the grasped object, the secondary DOF θ_2 is here constrained using a preloaded spring and a mechanical limit. In normal operation (*i.e.*, if no obstacles are encountered), this DOF is therefore not triggered and the leg endpoint follows the *free-space trajectory*, illustrated in Fig. 1b, solely generated by the rotation of θ_1.

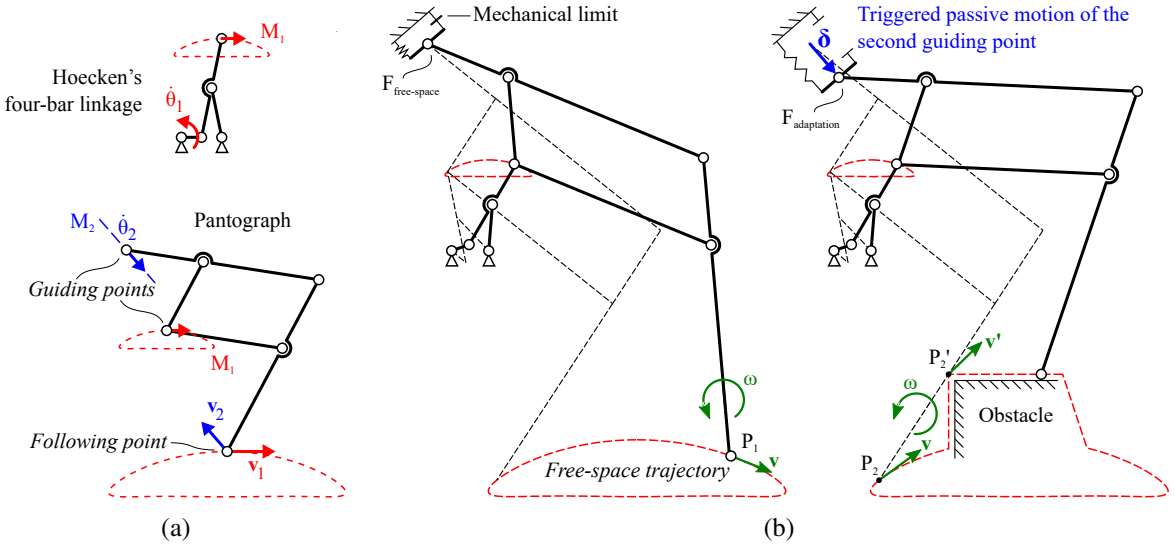

Fig. 1. Description of the mechanism's initial geometry: (a) constituent linkages, (b) simulation of the leg encountering an obstacle during its swing phase and subsequent passive adaptation

If a collision occurs during the swing phase of the leg motion, the continued actuation of θ_1 coupled with the obstacle resistance at the point of contact cause an increase of the mechanism's internal forces, which is used to overcome the preloaded spring. Then, the resultant motion of θ_2 combined to the rotation of θ_1 allows the leg endpoint to depart from the free-space trajectory and slide along the obstacle. Similarly to self-adaptive fingers, the spring acting on the θ_2 does not store any useful energy to the walk but only prevents incoherent motion of the leg endpoint, and resists the adaptation movement. In order to reduce the required actuation effort, the spring stiffness and preloading should therefore be kept as low as possible, *i.e.*, of the minimal magnitude required to balance the inertial effects to which point F is subjected. Since these effects are not apparent in the kinetostatic analysis performed in this paper, the selection of the spring is, for now, done during the initial testing of the physical linkage (for the first 3d-printed prototype, of total linkage mass of $\sim$100 g described in (Fedorov and Birglen, 2017), a spring with a stiffness of $k = 0.05$ N/mm and

an initial preload of 0.36 N was experimentally deemed suitable).

In Fig. 1b, the passive adaptation induces a translation (denoted by the vector $\boldsymbol{\delta}$) of the pantograph's guiding point, F, from its initial position ($F_{free-space}$) to a new location ($F_{adaptation}$). The displacement M_2 between these two points can be generated by any motion generator, the simplest choices being a prismatic joint (for which M_2 is a straight line) or a revolute one (for which M_2 is an arc), as in (Fedorov and Birglen, 2017). The nature of this generator is however left arbitrary.

Due to the geometry of the pantograph linkage, the vertical component of $\boldsymbol{\delta}$ must be negative to generate a rising motion of the leg endpoint. A purely vertical translation of F would therefore seem advantageous, but such a design would render the passive adaptation much more difficult, as will be shown in Section 3.1. At the other extreme, a completely horizontal $\boldsymbol{\delta}$ makes adaptation very easy, but could not result in the desired vertical motion of the leg endpoint along an obstacle. An intermediate orientation as illustrated in Fig. 1b must therefore be selected for the allowed range of motion of point F.

2.3. Initial geometric parameters

Although several straight line linkages can be suitable for the generation of the free-space trajectory, the Hoecken's linkage, with only three links, was selected here for its simplicity. Its geometric parameters are presented in Fig. 2 (h_1 and w_1 refer respectively to the trajectory's height and width) and Table 1, where l_{ij} refers to the distance between points i and j.

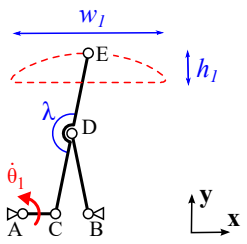

Fig. 2. Hoecken's linkage

Geometric parameter	Value
Coordinates of A	(0.00 0.00)
Coordinates of B	(2.00 0.00)
l_{AC}	1.00
l_{BD}=l_{CD}=l_{DE}	2.50
λ	180°

Table 1. Initial geometry (four-bar)

Next comes the dimensioning and positioning of the pantograph. The geometry of this linkage can be described using only two ratios:

- ρ is the amplification ratio which relates the sizes of similar triangles FGE and FHJ (see Fig. 3).
- α is the shape factor of triangles FGE and FHJ, defined as the ratio of l_{EG} to l_{FG} (see Fig. 3 again).

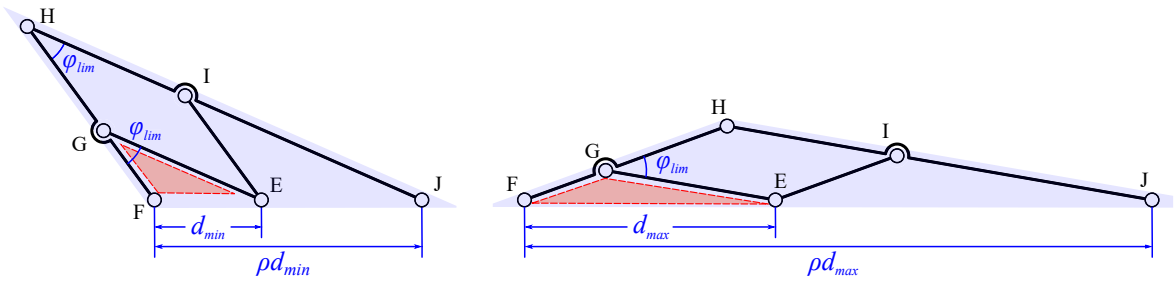

(a) (b)

Fig. 3. Geometry of the pantograph linkage with the guiding points either at their (a) closest or (b) farthest allowed positions

An important consideration when designing the mechanical leg is to prevent the pantograph from reaching a singular configuration, of which an indicator is the shape of the parallelogram EGHI: neither of its angles should be allowed to become smaller than a threshold value defined by ϕ_{lim}. This condition allows to set a design constraint on the permissible values of d, the distance between the guiding points E and F. First, the law of cosines is used with triangle EFG in both limit configurations illustrated in Fig. 3, *i.e.*:

$$d_{min}{}^2 = l_{FG}^2 + l_{EG}^2 - 2 \cdot l_{FG} \cdot l_{EG} \cdot \cos(\phi_{lim}) \tag{1a}$$

$$d_{max}{}^2 = l_{FG}^2 + l_{EG}^2 - 2 \cdot l_{FG} \cdot l_{EG} \cdot \cos(\pi - \phi_{lim}). \tag{1b}$$

Eqs. (1a) and (1b) can be combined using the previously defined ratio α to establish yet another ratio, d_{max}/d_{min}, which is maximal when $\alpha = 1$, *i.e.*, FGE and FHJ are isosceles triangles:

$$\frac{d_{max}}{d_{min}} = \sqrt{\frac{1 + \alpha^2 + 2\alpha \cdot \cos(\phi_{lim})}{1 + \alpha^2 - 2\alpha \cdot \cos(\phi_{lim})}}. \tag{2}$$

The position of point E, one of the pantograph's guiding points, is always the location of the four-bar's coupler point. Therefore, only six parameters remain unknown for the design of the pantograph:

- The x and y coordinates of $F_{free-space}$, the location of guiding point F during the free-space trajectory.
- The x and y coordinates of $F_{adaptation}(max)$, the location guiding point F at the maximal position in the chosen range of θ_2.
- The pantograph's ρ and α ratios.

As illustrated in Fig. 4, a translation $\boldsymbol{\delta}_{max}$ of F from $F_{free-space}$ to $F_{adaptation}(max)$ results in a shift of all the points of the free-space trajectory by vector $(\rho - 1)\boldsymbol{\delta}_{max}$, thereby defining the maximal adaptation trajectory.

Both the free-space and maximal adaptation trajectories have an identical shape to the Hoecken's linkage output curve, but scaled up to a height $h_2 = \rho h_1$ and a width $w_2 = \rho w_1$.

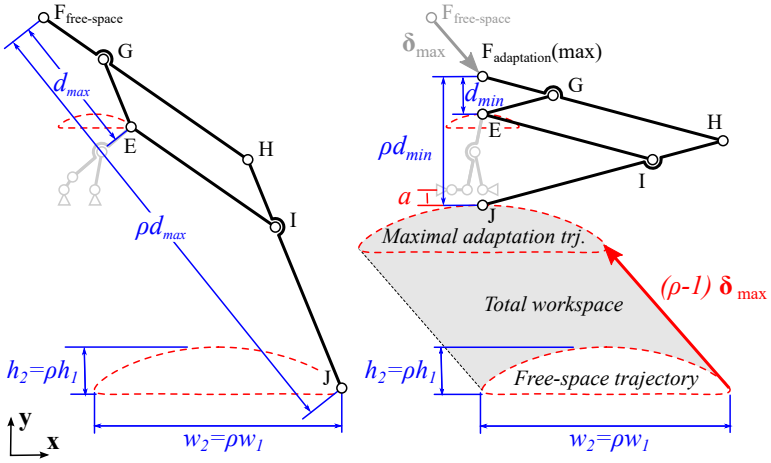

Fig. 4. Dimensioning of the pantograph, (a) $F = F_{free-space}$, (b) $F = F_{maximal\ adaptation}$

Geometric parameter	Value
Coordinates of $F_{free-space}$	(-1.33 11.17)
Coordinates of $F_{max.adaptation}$	(2.00 7.35)
$l_{EG} = l_{FG} = l_{HI}$	4.73
$l_{EI} = l_{GH} = l_{IJ}$	11.40

Table 2. Initial geometry (pantograph)

To ensure a unique solution for the dimensioning of the pantograph, which simplifies the subsequent optimization, six constraints have been selected. Using Fig. 4 as a reference, these constraints are listed below:

- Ensure a sufficiently large *total workspace* (*i.e.*, the area theoretically reachable by the leg's endpoint following motions of θ_1 and θ_2).

  $\Rightarrow$ *Constraint* C_1: the vertical distance $(\rho - 1)\boldsymbol{\delta}_{max}{}^T\mathbf{y}$ between the free-space and maximal adaptation trajectories is arbitrary chosen to be three times the height h_2 of the free-space trajectory:

$$(\rho - 1)\boldsymbol{\delta}_{max}{}^T\mathbf{y} = 3h_2. \tag{3}$$

- Allow for easy passive adaptation of the leg to collisions. As will be detailed in Section 3.1, the orientation of $\boldsymbol{\delta}$ has a critical effect on the torque required for the leg to slide along the surface of an obstacle. A compromise must be selected between the ease of adaptation and the proportion of the workspace located directly above the free-space trajectory.

  $\Rightarrow$ *Constraint* C_2: the horizontal distance $(\rho - 1)\boldsymbol{\delta}_{max}{}^T\mathbf{x}$ between the free-space and maximal adap-

tation trajectories is arbitrarily chosen at half the width w_2 of the free-space trajectory:

$$(\rho - 1)\boldsymbol{\delta}_{max}{}^{T}\mathbf{x} = w_2/2. \tag{4}$$

- Prevent interference between the leg's endpoint and Hoecken's linkage.

  $\Rightarrow$ *Constraint* C_3: the maximal adaptation trajectory is below the lower limit of the four-bar's envelope. For the Hoecken's linkage, the distance a between the origin and the maximal adaptation trajectory, c.f. Fig. 4, is therefore chosen equal to the length of the crank:

$$a = l_{ac}. \tag{5}$$

- Keep the mechanism as compact as possible.

  $\Rightarrow$ *Constraint* C_4: the centers of the maximal adaptation trajectory and that of M_1, the trajectory generated by the Hoecken's linkage, are horizontally aligned.

  $\Rightarrow$ *Constraint* C_5: the shape factor α of the pantograph is set at 1.

- Avoid singularities for all possible configurations of the mechanism.

  $\Rightarrow$ *Constraint* C_6: the limit angle ϕ_{lim} is set at 30° and Eq. (2) thus becomes:

$$\frac{d_{max}}{d_{min}} = 3.73. \tag{6}$$

The numerical parameters chosen for constraints C_1 and C_2 have here been arbitrary selected to demonstrate the subsequent geometry optimization procedure, but can be altered depending on specific requirements for the mechanism. The unique geometric parameters satisfying these six constraints for the Pantograph linkage are computed using an iterative method and are shown in Fig. 4 and Table 2 (the origin is still coincident with point A of the four-bar).

3. PERFORMANCE EVALUATION

3.1. Ease of adaptation

The actuation torque τ_{in} (acting on θ_1) required to perform the normal motion as well as the adaptation described in Section 2.2 can be expressed as a function of the preloading force f_p (acting on θ_2), the friction coefficient μ at the obstacle contact location, and the mechanism's configuration at the moment of this contact. This relationship can be found out by performing a static analysis on the mechanism. Two classes of contacts can be defined: in a *Type I* contact, the collision occurs at the leg endpoint and the orientation of the normal unit vector **n** at this point depends on the obstacle, whereas, in a *Type II* contact, collision occurs elsewhere along the terminal link of the leg and the orientation of the latter changes **n**. In both cases, the unit vector **t** is defined tangent to the relative sliding motion of the leg and the obstacle (c.f. Fig. 5).

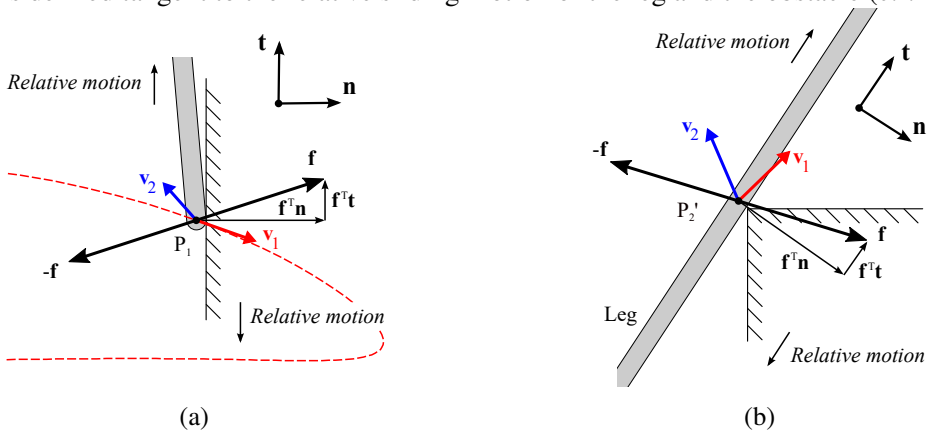

Fig. 5. Velocities and forces at the contact points, with either (a) *Type I* or (b) *Type II* contacts.

Using a Coulomb friction model with a coefficient μ and considering the edge of the friction cone, the contact force **f** is first expressed as:

$$\mathbf{f}^T\mathbf{t} = \mu\mathbf{f}^T\mathbf{n}. \tag{7}$$

For a *Type I* contact, **f** can also be written as:

$$\mathbf{f} = \mathbf{J}^{*-T}\boldsymbol{\tau}, \tag{8}$$

where $\boldsymbol{\tau} = \begin{bmatrix} \tau_{in} & -f_p \end{bmatrix}^T$ and $\mathbf{J}^*$ is a square submatrix of the mechanism's Jacobian, mapping the endpoint

linear velocity $\mathbf{v}$ to the velocities of the DOFs, *i.e.*,:

$$\mathbf{v} = \mathbf{J}^* \dot{\boldsymbol{\theta}} = \begin{bmatrix} \mathbf{v}_1 & \mathbf{v}_2 \end{bmatrix} \dot{\boldsymbol{\theta}}, \tag{9}$$

with $\dot{\boldsymbol{\theta}} = \begin{bmatrix} \dot{\theta}_1 & \dot{\theta}_2 \end{bmatrix}^T$. The matrix $\mathbf{J}^*$ can be interpreted geometrically as $\begin{bmatrix} \mathbf{v}_1 & \mathbf{v}_2 \end{bmatrix}$ where $\mathbf{v}_i$ is the derivative of the leg endpoint's position with respect to $\dot{\theta}_i$. As illustrated in Fig. 5a, $\mathbf{v}_1$ is always tangent to the freespace trajectory while the orientation of $\mathbf{v}_2$ is tangent to M_2, the motion associated to θ_2. More specifically, if a prismatic joint is used for M_2 its direction would be parallel to the vector $\boldsymbol{\delta}$. For a *Type II* contact, one can similarly define local velocities $\mathbf{v}_i$ by evaluating $\mathbf{J}^*$ at point P' which can be very conveniently obtained using screw theory (Davidson and Hunt, 2004).

Eqs. (7) to (9) can then be rearranged to yield the expression of the actuation torque required to overcome the preloading of the triggered motion:

$$\tau_{in} = \frac{-{\mathbf{v}_1}^T(\mathbf{n} + \mu\mathbf{t})}{{\mathbf{v}_2}^T(\mathbf{n} + \mu\mathbf{t})} f_p. \tag{10}$$

One might think that an easy way to decrease the ratio τ_{in}/f_p would be to maximize the dot product ${\mathbf{v}_2}^T(\mathbf{n} + \mu\mathbf{t})$, which is the denominator of Eq. (10), by making $\mathbf{v}_2$ parallel to $\mathbf{n}$. If a vertical obstacle and the generation of M_2 by a prismatic joint are assumed, this strategy would be equivalent to making the vector $\boldsymbol{\delta}$ horizontal. In turn, this would result in an unacceptable reduction of the available workspace directly above the free-space trajectory, which explains the compromise imposed by the pantograph design constraints C_1 and C_2.

Impact mechanics are neglected for the calculation of the required torque. Indeed, the worst case scenario is that, following a collision, the leg is forced to a standstill due to the impact forces and the inertial effects. However, the static conditions, for which Eq. (10) is derived, thereby become valid.

An example of the predicted evolution of the input torque during the sliding motion of the leg following a *Type II* contact, calculated for the initial geometric parameters assuming $\mu = 0$, is shown in Fig. 6. The maximal value of τ_{in}/f_p is in this case 8.21 at the very beginning of the sliding motion when the leg has not yet departed from the free-space trajectory. This maximal value quantifies the ease of adaptation to any obstacle for which a contact would be established at this particular point.

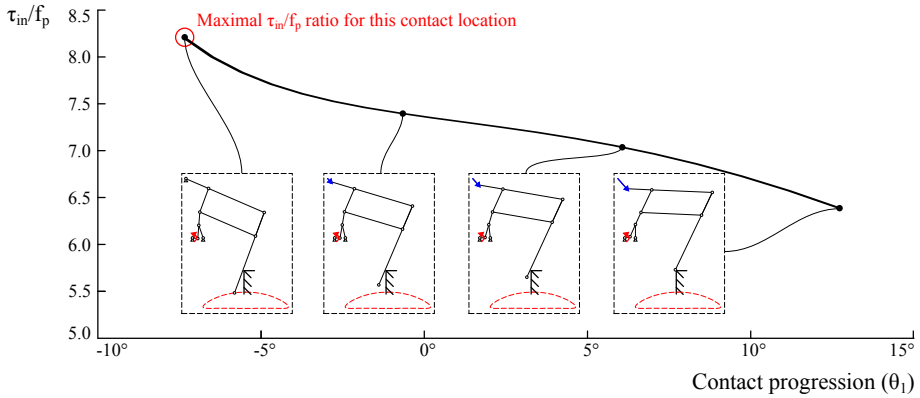

Fig. 6. Required input torque for an adaptation following a *Type II* contact with $\mu = 0$ and a collision point at $(9.5, -6.0)$

A similar contact simulation can be performed for all possible collision points as illustrated in Fig. 7a. These points form the *adaptation workspace*, which is a smaller subset of the total workspace (points reachable by the endpoint following rotations of θ_1 and θ_2). Indeed, no collision can occur at points located above the terminal link, such as point P in Fig. 7a, since they are not swept by the leg during normal motion along the free-space trajectory. A variation of the initial geometry is therefore introduced to increase the area of this adaptation workspace, referred to as the *workspace-maximizing shape*, in which the terminal link is altered so that it is vertical at the beginning of the swing phase. This increases the range of possibly overcomable obstacles (c.f. Fig. 7b). It is important to note that altering the shape of this link without changing the coordinates of the joints still affects the τ_{in}/f_p ratio since the contact location and the orientation of $\mathbf{n}$ are different. Indeed, all possible obstacle contacts occur at the endpoint (*Type I*) for the workspace-maximizing shape which has the drawback of increasing the required input torques for adaptation.

Since it is numerically faster to evaluate the required torque for *Type I* contacts, the adaptation performance index I_{adap} proposed here is based on the workspace-maximizing shape of the terminal link. Assuming vertical obstacles ($\mathbf{n} = [1\ 0]^T$) and no friction ($\mu = 0$), the τ_{in}/f_p ratio is evaluated for all points comprising the swing phase of the free-space trajectory, as plotted in Fig. 8, based on the geometry illustrated in Fig. 7b. The value of I_{adap} is defined as the root mean square (RMS) of the ratio τ_{in}/f_p along this curve, which is equal to 6.23 for the initial geometry of this particular example. A maximal ratio of 10.56 is reached at point Q, illustrated in Fig. 7b.

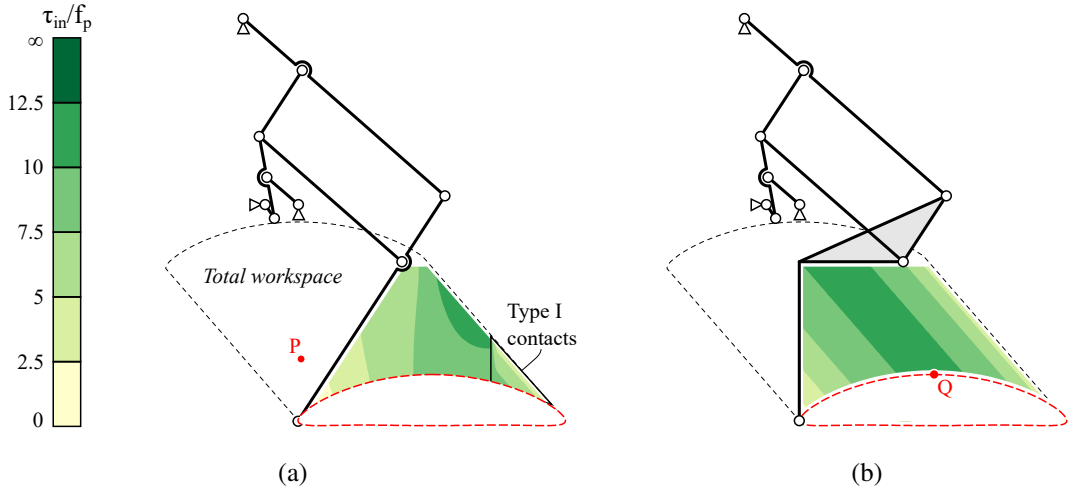

Fig. 7. Required input torque for all possible collision points with $\mu = 0$, and different shapes of the terminal link: (a) straight terminal link, (b) workspace-maximizing shape with $\mathbf{n} = [1\ 0]^T$

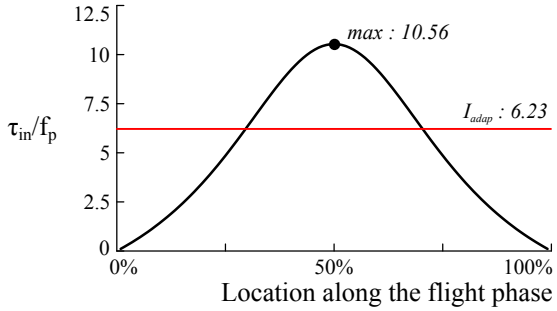

Fig. 8. Evaluation of I_{adap} for the initial geometry

While this index assumes, for comparison purposes, only frictionless endpoint contacts with vertical obstacles, which might not be realistic in practical applications, there still exists a direct correlation between I_{adap} and the torque required for the terminal link to slide along an obstacle. A discussion of the mechanism's adaption to specific obstacles follows in Section 5.

Moreover, other than the trade-off between the adaptation workspace area and the required torque for adaptation, there exists an important reason to favoring link (*i.e.*, *Type II*) rather than endpoint (*i.e.*, *Type I*) contacts with obstacles: potential interference *after* a successful adaptation. An interference is here defined as a contact on the back of the leg which prevents it from returning to the free-space trajectory. This effect, illustrated in Fig. 9, is even more pronounced when the pantograph is operated in what is referred to, in the literature, as the "ostrich mode" (Ottaviano et al., 2005), *i.e.*, the pantograph's links are located aft of the guiding points.

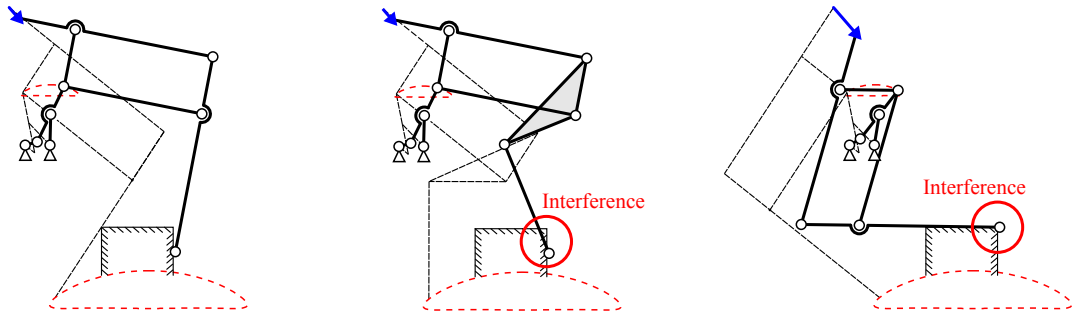

Fig. 9. Possible interference between the pantograph and the obstacle after adaptation: (a) straight terminal link, no interference (b) workspace-maximizing terminal link, slight interference, (c) "ostrich" pantograph configuration, important interference.

3.2. Free-space trajectory

The quality of the free-space trajectory is a another key element to consider during the design. The associated performance index is, in addition to I_{adap}, a second basis for comparison between various geometries. Since this trajectory is only a scaling-up of M_1, generated by the four-bar linkage, it is easier to directly evaluate the latter. To this aim, three criteria scored on a scale from 0 to 100% are defined:

• **Stance phase linearity**: the vertical difference Δh between the top and bottom points of the stance phase is compared to the total height h_2 of the trajectory (in order to account for the transition between swing and stance phases, their widths are arbitrarily set at 95% of w_2, the total trajectory width, as shown in Fig. 10):

$$lin\% = \left(1 - \frac{\Delta h}{h_2}\right) \times 100\% \tag{11a}$$

• **Stance phase ratio**: the fraction of the input crank cycle that is spent in the stance phase is compared with the target fraction chosen at 0.6:

$$sta\% = min\left(\left(\frac{\text{stance duration}}{0.6}\right), 1\right) \times 100\% \tag{11b}$$

• **Height-to-width ratio**: in order to penalize designs generating trajectories flatter than that of the Hoecken's linkage ($h_1/w_1 = 0.19$), the height-to-width ratio is compared to this latter value:

$$hwr\% = min\left(\left(\frac{h_1/w_1}{0.19}\right), 1\right) \times 100\% \tag{11c}$$

A free-space trajectory quality index I_{trj} combining the stance phase linearity, stance phase ratio, and height-to-width ratio criteria into a single performance index is then defined:

$$I_{trj} = 1 - \frac{lin\%}{100\%} \cdot \frac{sta\%}{100\%} \cdot \frac{hwr\%}{100\%} \tag{12}$$

Table 3 details the calculation of I_{trj} for the initial geometric parameters listed in Table 1. The obtained value, 0.03, is excellent although the mechanism fared much worse when its passive adaptation was evaluated, with an I_{adap} of 6.23. It is of course impossible to minimize simultaneously both indices to satisfy the two very different objectives, and a compromise between them must be investigated.

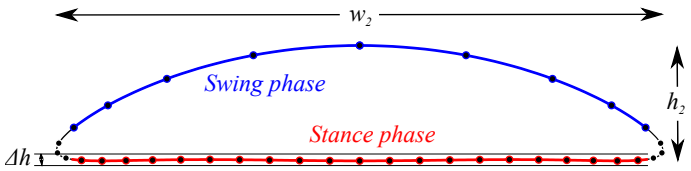

Fig. 10. Hoecken's linkage trajectory, with points drawn each 10° rotation of the input crank.

Linearity score	98.6%
Stance ratio score	98.3%
Height-to-width score	100%
I_{trj}	**0.03**

Table 3. Evaluation of I_{trj} for the initial geometry

4. OPTIMIZATION OF THE GEOMETRY

Having defined two conflicting performance indices, a multi-objective optimization can be performed on a search space comprising all possible linkages generating the trajectory M_1, in order to visualize the associated Pareto front. For the candidate geometries comprising the Pareto set, *i.e.*, located on this front, a decrease of one objective function can only lead to an increase of the other, so their overall merits depend solely on the relative importance given to these two criteria.

For the purpose of this optimization, the search space is limited to the parameters of the crank-rocker four-bar linkage, the geometry of which is defined by three variables: l_{AB}, l_{CD} and l_{BD}. Two additional variables, l_{DE} and λ, position the coupler point E which is connected to the pantograph. Table 4 describes the allowed ranges for these variables, which, along with the inequality constraints defined in Eqs. (13a-c), ensure that

the unit-length crank is able to perform a full revolution without encountering a singular configuration.

Variable	Description	Limits	Inequality Constraints	
l_{AB}	Base link length	$1.1-10$		
l_{CD}	Coupler link length	$1.1-10$	$l_{AB}+l_{BD}>l_{CD}+1$	(13a)
l_{BD}	Rocker link length	$1.1-10$	$l_{CD}+l_{BD}>l_{AB}+1$	(13b)
l_{DE}	Additional distance to coupler point	$0.1-10$	$l_{AB}+l_{CD}>l_{BD}+1$	(13c)
λ	Coupler link shape	$0-2\pi$		

Table 4. Conditions for the generation of a suitable candidate geometry

As described by the flowchart shown in Fig. 11, both indices I_{trj} and I_{adap} are assigned to a candidate four-bar linkage by first determining its optimal orientation, minimizing I_{trj}, and then, generating the unique pantograph linkage satisfying constraints C_1 to C_6 (previously described in Section 2.3) for this particular four-bar, which allows to compute I_{adap}.

Due to the highly non-linear nature of the problem, a genetic algorithm provided by `MATLAB`'s *Optimization Toolbox* was used with the parameters described in Table 5 to explore the search space and find near-optimal solutions. The fitness of the best individuals obtained after 100 generations is plotted in Fig. 12.

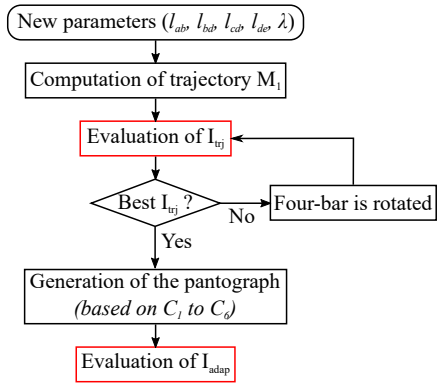

Fig. 11. Evaluation sequence of a candidate geometry

Multi-Objective Genetic Algorithm	
Number of iterations	100
Population size	100
Pareto population limit	35
Crossover fraction	0.8
Crossover mechanism	Randomly weighted average
Mutation function	`Matlab`'s Adaptive Feasible algorithm
Selection mechanism	Best of 4 randomly selected individuals
Deterministic Nonlinear Optimization Algorithm	
Algorithm	Sequential Quadratic Programming
Function evaluations	357

Table 5. Parameters of the optimization algorithms

Conversely to usual optimization techniques, a genetic algorithm allows to optimize simultaneously both objectives by keeping a large population of candidate geometries instead of a single one. Moreover, this approach allows to avoid the pitfalls of local minima, which the function can be shown to possess. Indeed, as an example, a specific geometry has been selected from the Pareto set for further analysis. As illustrated in Fig. 12, this geometry, indicated by "X" in the figure, is located at (or very close to) the global minimum for

the particular optimization function $I = 3.63I_{trj} + I_{adap}$. However, a deterministic minimization algorithm (described in Table 5) applied to the latter function with the initial geometry as starting point does not converge towards this global minimum, but towards a local minimum, identified by "+" in the figure, see Table 6.

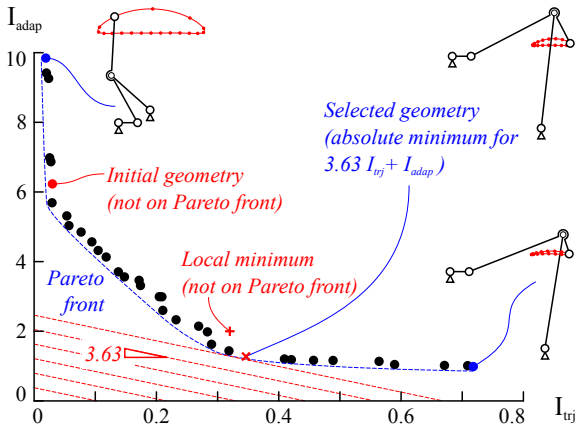

Fig. 12. Pareto set found after 100 generations

Parameter	Initial Geo.	Selected Geo.	Local Min.
l_{AB}	2	6.08	5.23
l_{CD}	2.5	4.99	8.90
l_{BD}	2.5 0	6.17	10.00
l_{DE}	2.5	1.82	3.73
λ	180°	270°	302°
I_{trj}	0.03	0.35	0.32
I_{adap}	6.23	1.27	2.01
$3.63I_{trj} + I_{adap}$	6.34	2.53	3.17

Table 6. Optimization results

5. ANALYSIS OF THE SELECTED GEOMETRY

The arbitrarily selected geometry (described in Fig. 13 and Table 7) features a remarkable improvement of I_{adap} from 6.23 to 1.27 at the cost of a deterioration of I_{trj} from 0.03 to 0.35 compared to the initial parameters. The ease of adaptation can be further improved by using a straight terminal link, which would ensure *Type II* contacts for a large portion of the swing phase.

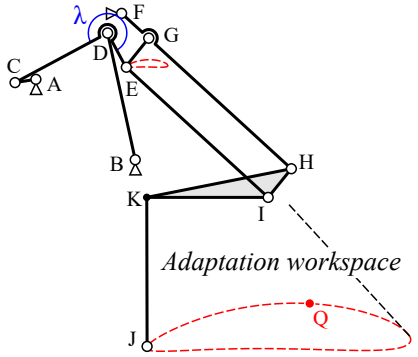

Fig. 13. Illustration of the selected geometry

Geometric parameter	Value	Geometric parameter	Value
Coord. of A	(0 0)	l_{AC}	1.00
Coord. of B	(4.72 -3.83)	l_{BD}	6.17
Coordinates of $F_{free-space}$	(4.08 3.14)	l_{CD}	4.99
		l_{DE}	1.82
Coordinates of $F_{max.adaptation}$	(5.27 1.84)	$l_{EG} = l_{FG} = l_{HI}$	1.75
		$l_{EI} = l_{GH} = l_{IJ}$	9.19
		λ	270°

Table 7. Geometric parameters of the selected design

As is clear from Fig. 14 and Table 8, the main drawback of this design is the reduction of the stance phase duration from 59% to 44% of the leg cycle. A possible solution could be to increase the number of legs, or

to alter the angular velocity of the input crank using, for instance, non-circular gears or cams.

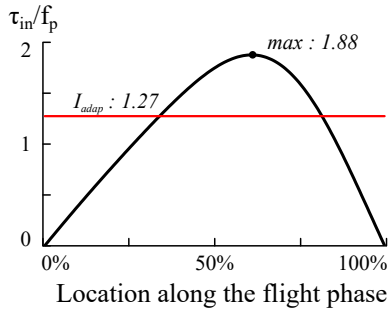

(a)

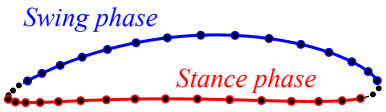

(b)

Fig. 14. Evaluation of (a) I_{adap} and (b) I_{trj} for the selected design. Points are drawn each 10° rotation of the input crank.

Linearity	93.3%
Stance ratio	73.4%
Height-to-width ratio	95.4%
I_{trj}	**0.35**
I_{adap}	**1.27**

Table 8. Summary of the performance indices

The improved adaptation capabilities can be further demonstrated by comparing the required torque for adaptation at the most critical point of the swing phase for the initial and selected geometries, *i.e.*, point Q in Figs. 7b and 13. The effect of the obstacle angle and friction coefficient on *Type I* contacts, described by Eq. (10), is plotted for both geometries in Fig. 7. Depending on the friction coefficient, adaptation in the desired direction is shown to be possible even for overhanging obstacles, *i.e.*, whose normal has a downwards component.

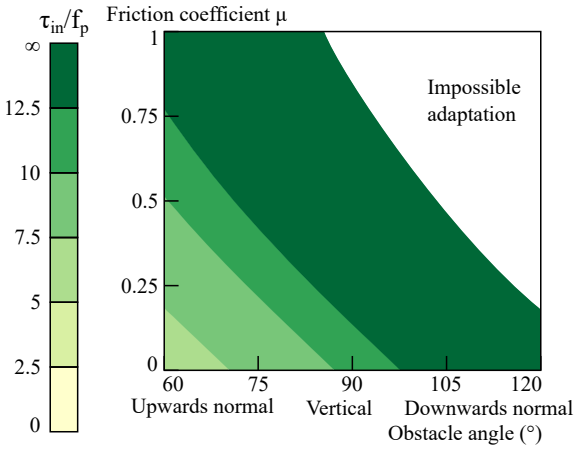

(a)

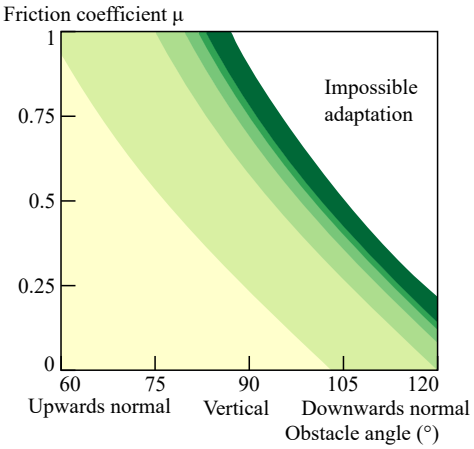

(b)

Fig. 15. Influence of obstacle angle and friction coefficient on the adaptation torque ratio at point Q: (a) initial geometry, (b) selected geometry

Adaptation to this latter type of obstacles has been investigated with the help of the MSC *Adams* dynamic simulation package. Since only a single leg was simulated, the influence of the rest of mechanism was represented by constant vertical position and only positive horizontal motion constraints for the mechanism

body. The latter is a conservative hypothesis, since during the swing phase of a given leg, the other legs usually actively push the body of a multi-legged robot forwards.

Fig. 16a shows obstacle adaptation for a straight terminal link, resulting in a *Type II* contact. After the adaptation, the leg endpoint returns to the free-space trajectory by following a direction parallel to δ, and the next step is initiated. In Fig. 16b, the leg slides upwards along the obstacle, as predicted, even if the first contact point has a downwards normal. There is however a slight interference after the adaptation, to which the mechanism reacts by moving forwards, resulting in a sliding of point K along the obstacle. This does not cause the mechanism to get stuck during the next step, since the terminal link then undertakes a rotation around its extremity, *i.e.*, the contact point with the ground. A video of the simulations is available online at `www.youtube.com/watch?v=-ArcRu-ErvA`.

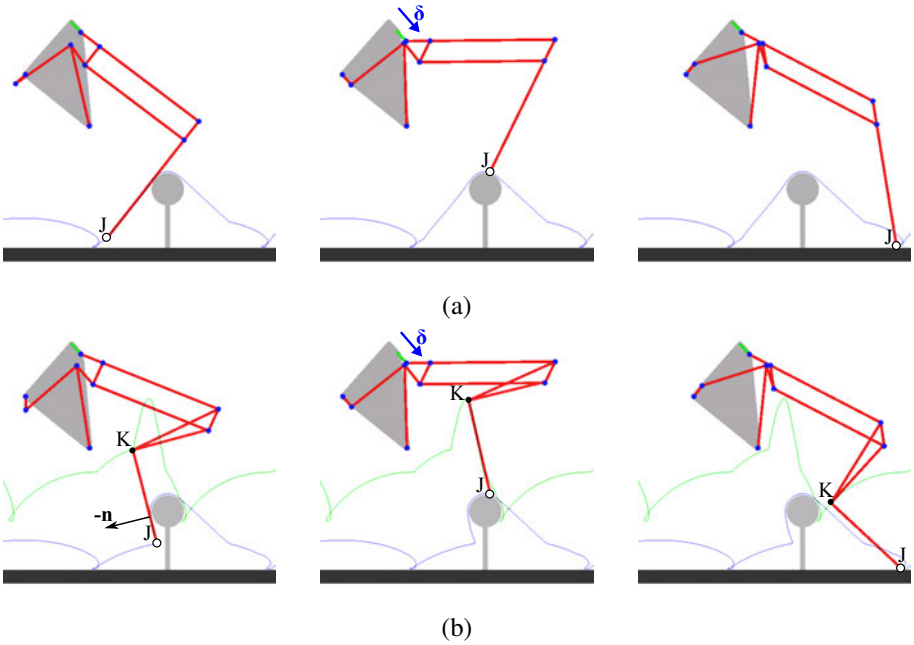

Fig. 16. Mechanism simulation using `MSC Adams` : Obstacle adaptation with a) a straight terminal link b) the workspace-maximizing terminal link

6. CONCLUSIONS

In this paper, the passive reconfiguration of a Hoecken's-Pantograph robotic leg mechanism due to the use of a second triggered DOF, in a similar manner as underactuated mechanical fingers, is investigated. The geometric parameters of the mechanism were optimized in order to allow it to efficiently slide along obstacles following contacts occurring during its swing phase while retaining an efficient free-space trajectory for the

leg endpoint, and the Pareto front representing the trade-off between these objectives was highlighted.

ACKNOWLEDGMENTS

The support of the Natural Sciences and Engineering Research Council (grant RGPIN327005) is gratefully acknowledged.

REFERENCES

L. Birglen. Type synthesis of linkage-driven self-adaptive fingers. *Journal of Mechanisms and Robotics*, 1(2):021010, 2009.

L. Birglen, T. Laliberté, and C. Gosselin. *Underactuated Robotic Hands*. Springer, New York, 2008.

J. K. Davidson and K. H. Hunt. *Robots and screw theory*. Oxford University Press, Oxford, 2004.

D. Fedorov and L. Birglen. Design of a self-adaptive robotic leg using a triggered compliant element. *IEEE Robotics and Automation Letters*, 2(3):1444–1451, 2017.

M. Focchi, V. Barasuol, I. Havoutis, J. Buchli, C. Semini, and D. G. Caldwell. Local reflex generation for obstacle negotiation in quadrupedal locomotion. In *Proc. Int. Conf. Climbing Walking Robots*, pages 443–450, 2013.

M. Hutter, C. Gehring, M. Bloesch, M. A. Hoepflinger, C. D. Remy, and R. Siegwart. Starleth: A compliant quadrupedal robot for fast, efficient, and versatile locomotion. In *15th International Conference on Climbing and Walking Robot-CLAWAR 2012*, number EPFL-CONF-181042, 2012.

H. Khakpour, L. Birglen, and S.-A. Tahan. Synthesis of differentially driven planar cable parallel manipulators. *IEEE Transactions on Robotics*, 30(3):619–630, 2014.

C. Liang, M. Ceccarelli, and Y. Takeda. Operation analysis of a chebyshev-pantograph leg mechanism for a single dof biped robot. *Frontiers of Mechanical Engineering*, 7(4):357–370, 2012.

S. Nansai, N. Rojas, M. R. Elara, R. Sosa, and M. Iwase. On a jansen leg with multiple gait patterns for reconfigurable walking platforms. *Advances in Mechanical Engineering*, 7(3):1–18, 2015.

E. Ottaviano, M. Ceccarelli, and C. Tavolieri. Kinematic and dynamic analyses of a pantograph-leg for a biped walking machine. In *Climbing and Walking Robots*, pages 561–568. Springer, 2005.

H.-W. Park, A. Ramezani, and J.W. Grizzle. A finite-state machine for accommodating unexpected large ground-height variations in bipedal robot walking. *IEEE Transactions on Robotics*, 29(2):331–345, 2013.

U. Saranli, M. Buehler, and D. E. Koditschek. Rhex - a simple and highly mobile hexapod robot. *International Journal of Robotics Research*, 20(7):616–631, 2001.

C. Semini, N. G Tsagarakis, E. Guglielmino, M. Focchi, F. Cannella, and D. G. Caldwell. Design of hyq–a hydraulically and electrically actuated quadruped robot. *Proceedings of the Institution of Mechanical Engineers, Part I:*

Journal of Systems and Control Engineering, 225(6):831–849, 2011.

L. Tao and M. Ceccarelli. Additional actuations for obstacle overcoming by a leg mechanism. In S. Bittanti, A. Cenedese, and S. Zampieri, editors, *Preprints of the 18th IFAC World Congress*. Milan, Italy, 2011.